Journal of *Marine Science and Engineering*

MDPI

Article

Hydrodynamic Response to Current and Wind on a Large Floating Interconnected Structure

Sarat Chandra Mohapatra [1,*], Pouria Amouzadrad [1], Iuri Baldaconi da Silva Bispo [2] and C. Guedes Soares [1]

[1] Centre for Marine Technology and Ocean Engineering (CENTEC), Instituto Superior Técnico, Universidade de Lisboa, Av. Rovisco Pais, 1049-001 Lisboa, Portugal; pouria.amouzadrad@centec.tecnico.ulisboa.pt (P.A.); c.guedes.soares@centec.tecnico.ulisboa.pt (C.G.S.)

[2] ISCA, University of Aveiro, Campus Universitário de Santiago, 3810-193 Aveiro, Portugal; iuri.bispo@ua.pt

* Correspondence: sarat.mohapatra@centec.tecnico.ulisboa.pt

Abstract: A numerical hydrodynamic model for a moored interconnected floating large structure under the action of regular waves is presented to analyze the effect of current and wind. The floating structure consists of 20 hinged plates that are linked together and secured with mooring lines along its edges. A brief discussion is provided on the multi-body hydrodynamics equations related to the numerical model definitions in both the frequency and time domains. Conversely, a concise overview of the experiment is given. The numerical model outcomes of vertical displacements and wave quantities are compared against the results obtained from model test data sets and numerical and analytical models in a recent publication. A high degree of accuracy has been noted in reflection and transmission coefficients with a certain value of current velocity. The numerical model simulating interconnected structures of 10 and 16 hinged plates is analyzed, and the resulting vertical displacements under the influence of current are compared to those of a 20-hinged structure. The impact of currents and winds on the hydrodynamic response of the structure is examined by studying various results, using stiffness values for both mooring and hinges. Further, the effect of wavelengths on the wave transmission on every side of the interconnected structure through contour diagrams, hydrodynamic diffraction for different incident angles, and wave quantities on current speed are analyzed. It is observed that as the current speed rises, the structural displacement also escalates; meanwhile, no impact of the wind on the floating interconnected structure is noted. It has been observed that as the wave direction shifts from 0° to 60°, the interconnected floating structure experiences a slight reduction in wave motion throughout the entire system.

Keywords: hydrodynamic response; mooring lines; numerical model; current–wind effect; large floating structure; experiment; structural displacement; wave quantity

check for updates

Academic Editor: Constantine Michailides

Received: 14 December 2024
Revised: 29 December 2024
Accepted: 30 December 2024
Published: 1 January 2025

Citation: Mohapatra, S.C.; Amouzadrad, P.; Bispo, I.B.d.S.; Guedes Soares, C. Hydrodynamic Response to Current and Wind on a Large Floating Interconnected Structure. *J. Mar. Sci. Eng.* **2025**, *13*, 63. https://doi.org/10.3390/jmse13010063

Copyright: © 2025 by the authors. Licensee MDPI, Basel, Switzerland. This article is an open access article distributed under the terms and conditions of the Creative Commons Attribution (CC BY) license (https://creativecommons.org/licenses/by/4.0/).

1. Introduction

As the population and economy have surged, the demand for energy, resources, and space has also escalated. The utilization of marine resources and oceanic space has grown more prevalent. There is a constant flow of innovative large offshore structures being designed and implemented for various purposes, such as offshore oil and gas platforms, launch sites, renewable energy islands, platforms for tourism, aquaculture bases, and mobile offshore bases. The exploitation of the ocean is shifting to deeper and more remote waters, while the dimensions of offshore structures are also expanding. In recent years, a novel form of offshore structure has been developed: a substantial floating structure composed of multiple bodies, characterized by hinges and numerous plates or modules.

This design achieves significant dimensions by connecting multiple substructure units that share the same or similar design [1–4].

Research on multi-body hydrodynamics has been explored from various perspectives using numerical methods and numerical software. Under regular waves, the dynamic behaviour of a Very Large Floating Structure (VLFS) combined of five and sixteen modules based on the 2D and 3D approximate hydroelasticity theories was studied [5]. Under frequency domain analysis, the efficiency of multiple floating breakwaters linked with hinges subjected to linear waves was studied numerically [6]. Under the potential-flow-based numerical model, the hydrodynamic sensitivity of an articulated modular floating structure was analysed by using a weakly nonlinear Green function solver AQWA [7]. The dynamics responses of floating bodies based on the theoretical and numerical solution method were studied under the Boussinesq equations and Rankine source method [8]. The hydrodynamic coefficients and hydrodynamic loads of multiple rigid bodies with a connector–mooring coupled system were estimated based on the high-order finite element (FE) and using the conventional modal superposition method [9].

The dynamics of the multi-module floating structures were studied using the theory of potential flow and the Euler–Bernoulli beam assumption [10]. The floating airport's nonlinear dynamics, composed of several multi-modules connected with flexible connectors and mooring systems, were examined [11]. Subjected to regular waves, the impact of hinged connectors of two-dimensional floating plates (modelled as Mindlin plate theory) was studied over finite water depth [12]. The bending moment and structural deflection of the floating plate structures subjected to regular waves were analysed [13]. Under external loads, the transient response of an interconnected flexible structure was simulated based on a time domain method [14]. Boundary Integral Equation Method (BIEM) codes were developed to analyse the influence of the stiffness of mooring lines on the structural behaviour of a floating flexible plate in different water depths [15] and circular structures [16]. ANSYS AQWA was implemented to determine the RAOs and analyse the effect of winds on an integrated offshore fish cage and wind turbine [17]. The hydroelastic behaviour of the VLFS with porous, non-porous, or two submerged horizontal plates was analysed based on a numerical model [18]. The BEM was implemented to study the hydroelastic response of a VLFS edged with two inclined porous plates under oblique waves, and the results were validated against model tests [19]. The performance of the FC connector of a large modularized floating structure was studied based on the network modelling method and finite element method (FEM) [20].

In addition to the studies on the hydrodynamic and mechanical interactions of floating bodies, recent years have seen considerable focus on fluid resonance in confined spaces, which is discussed below. This phenomenon arises when an incoming wave aligns with the natural frequency of the fluid within these narrow gaps, leading to substantial amplitude oscillations at the free surface. Such oscillations can significantly influence wave loads and are deemed a crucial element in maintaining the safety of offshore operations and infrastructure. A 2D numerical wave flume was used to study the wave resonance phenomenon within the narrow gap that occurs between two boxes of different sizes [21]. An open-source OpenFOAM® (website: https://www.openfoam.com) computational fluid dynamics (CFD) package is employed to investigate the hydrodynamic characteristics of gap resonance within the gap formed between two adjacent boxes subjected to wave excitation [22,23]. The impact of incident wave direction on gap resonance and transient effects between closely spaced floating bodies was explored using BEM [24] and CFD for analysis [25]. An investigation was conducted by focusing on fluid resonance phenomena within narrow gaps in multi-box systems utilizing CFD simulations within the OpenFOAM® software (website: https://www.openfoam.com) [26]. A discrete module–finite element (DM-FE)

approach was developed within the frequency domain to investigate the hydroelastic response of large floating flexible structures (FFSs) characterized by intricate interconnected features [27]. Within the OpenFOAM® framework, the complex interactions between nonlinear waves and the multiple barge configurations were investigated to explore the influence of fluid resonance phenomena occurring within the gaps between the barges on the resulting hydrodynamic wave forces [28,29].

Another captivating feature of the interconnected multi-body floating structures is the exploration carried out through experimental model tests. The experiments play a crucial role in analysing the motion of floating articulated structures that mimic flexibility, which is an essential characteristic for structural analysis in engineering applications within the marine environment. The hydroelastic response of the floating structure was predicted based on analytical and model tests under wave conditions [30]. The hydrodynamic efficiency of a breakwater box shaped in a 2D wave flume was investigated and subjected to regular waves [31]. Further, the dynamic response of an eight-module VLFS was studied under different wave conditions based on model tests [32]. The impact of the connector on the dynamic characteristics of an articulated floating structure was studied by conducting model tests subjected to different wave conditions [33]. The model tests were performed for an articulated floating structure to analyse the motion characteristics based on the computer vision target tracking technique [34]. An experimental investigation on the resonant behaviour and the excitation within the narrow gap between two floating bodies was conducted [35]. An experimental study was conducted to examine the resonant response of two stationary vessels experiencing transient wave groups within a gap [36]. The motion response of hinged floating multi-bodies consisting of a series of uniform rectangular boxes was presented based on experimental and numerical investigations [37].

Based on the three-dimensional hydroelastic theory, the load connectors of a three-module VLFS in shallow water depth were studied using experimental and numerical methods [38]. Further, the hydroelastic behaviour of a VLFS of an eight-module structure was examined using a numerical method, and experiments were conducted [39]. The wave attenuation and dynamic analysis of a floating breakwater of kelp-box type were studied based on numerical and model tests [40]. A frequency–time domain model was presented to study the structural safety and seakeeping performance of VLFS using the rigid module flexible connector [41]. The hydrodynamic analysis of a VLFS model designed as multimodule structures linked by connectors was investigated based on experimental model tests [42]. Recently, a review of current research and model developments on hydroelastic response and gap resonance was presented [43]. A numerical ANSYS AQWA was implemented to design an articulated large floating flexible structure, and the structure dynamics were analysed by considering different design parameters [44].

In this paper, specifically, we present several new contributions that differ from those in [44], including (i) the re-simulation of a numerical model by integrating the effects of current speed and wind on hydrodynamic response; (ii) a comparison of the findings with results from experimental model tests, as well as numerical and analytical data; (iii) the simulation of numerical models for interconnected structures comprising 10 and 16 plates, with a focus on comparing the vertical displacement results in the presence of current against those of the 20-body model; (iv) the presentation of contour plots and analysis of hydrodynamic diffraction; and (v) a set of analysis on the influence of current speed on the reflection coefficient (K_r) and transmission coefficient (K_t).

Explicitly, the main content of this paper is organized as follows: under frequency and time domains, the boundary conditions and governing equations of the aforementioned model are briefly presented in Section 2. A brief description of the experiment of the model test is provided in Section 3. Section 4 compares the numerical simulations

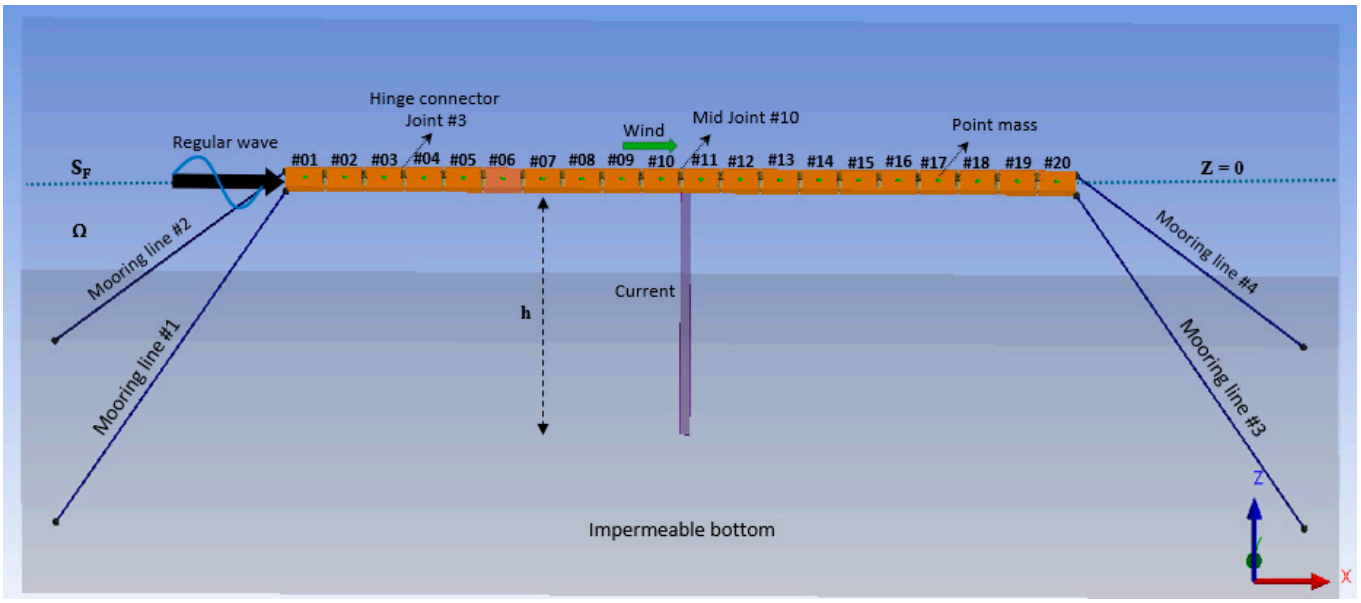
for structural displacements with experimental model results and, further, wave quantities with numerical and analytical results. Further, the impacts of varying structural and environmental parameters on the hydrodynamic response of the articulated floating structure displacement, RAOs, and wave transmission around the structure via contour plots are described. Additionally, hydrodynamic diffraction is analyzed by studying different numerical simulations on the various wave directions from 0 to 60 degrees. The impact of current speed along with mooring stiffness, water depth, and rotational stiffness on the reflection coefficient K_r and transmission coefficient K_t are presented and results are analyzed. Section 5 provides a concluding overview of this study's findings and identifies promising avenues for further investigation.

2. Description and Formulation of Numerical Model

2.1. Description

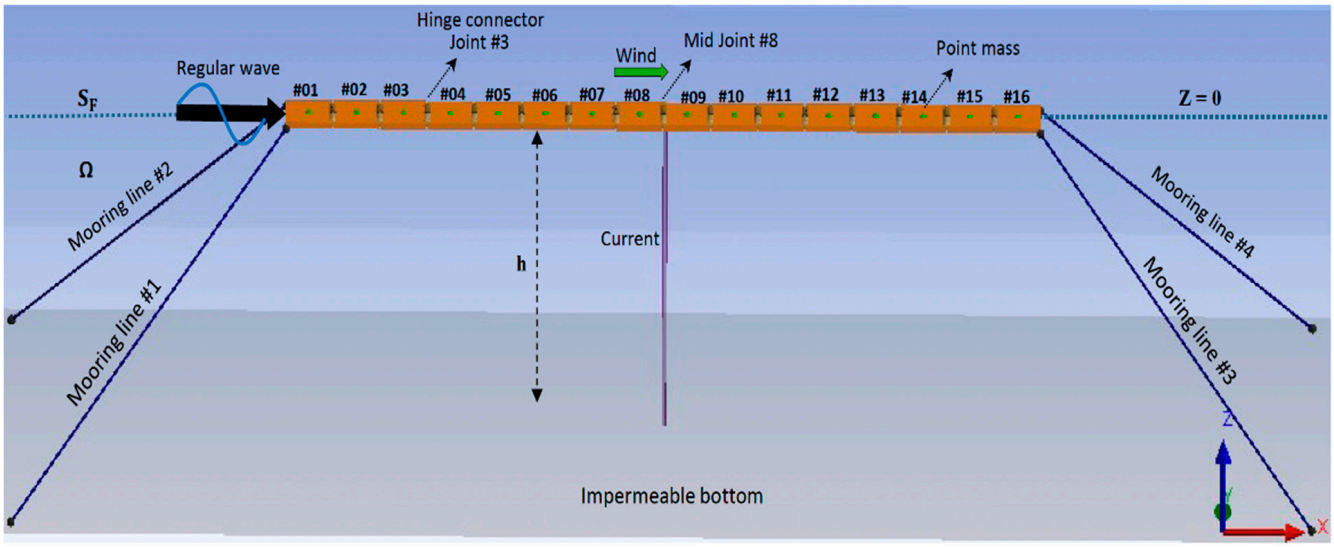
ANSYS AQWA (version: 2022 R2) is utilised to model the response of a moored interconnected floating structure in regular waves with hinge connectors with one DOF about the x-axis. Figure 1 displays a graphical illustration of the integrated multi-body system, which includes plates, hinges, and mooring lines and indicates current and wind phenomena. In addition to the structural geometry, the hinges for interconnections are illustrated as vertical cylinders in two shades of brown placed between the plates. The green spheres indicate the centre of mass for each plate, while the black spheres denote fixed positions that serve as connection points for the plates and mooring lines (see Figure 1a for 20 hinged plates, Figure 1b for 16 hinged plates, and Figure 1c for 10 hinged plates).

This numerical model incorporates only head waves. The water bottom is presumed to be both uniform and impermeable. Hydrodynamic parameters are established for frequencies that match wave periods ranging from $T = 2$ s to $T = 60$ s. The overall design parameters of the current model are the same as in [45] and the new environmental parameters are current speed (m/s) V = 0.5 to 2.0 and wind speed (m/s) U = 0 to 5.

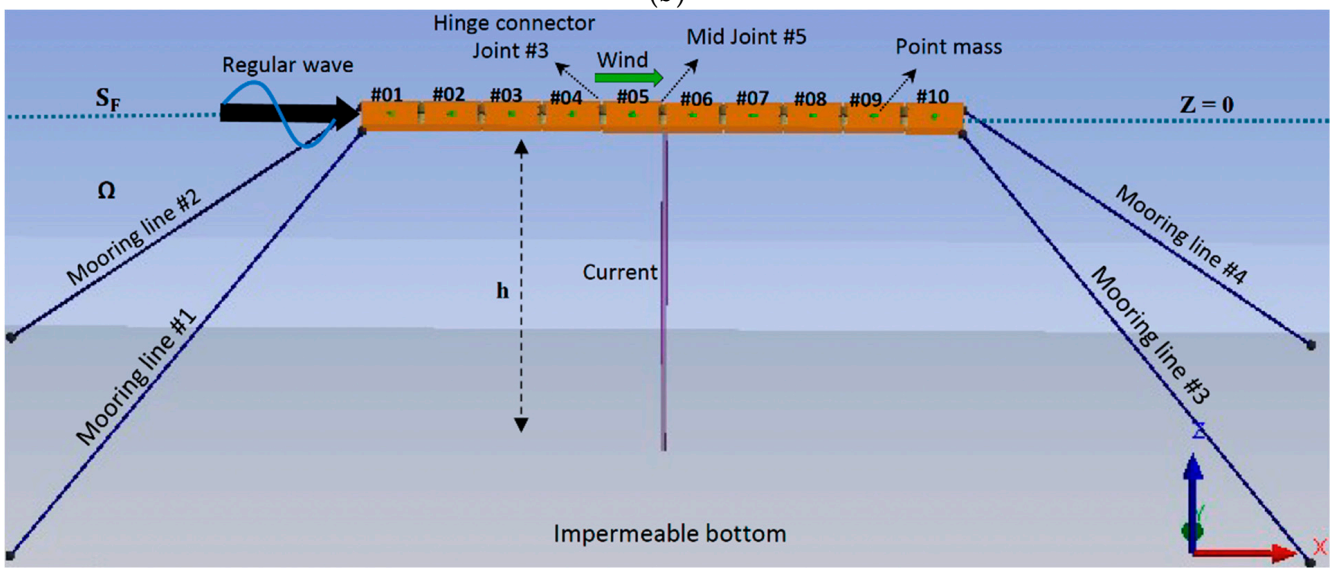


(**a**)

Figure 1. *Cont.*



(**b**)



(**c**)

Figure 1. (**a**) Numerical setup of interconnected floating structure (20 bodies; #01,#02, . . ., #20) with current and wind loads. (**b**) Numerical model of 16 hinged plates (#01, #02,. . ., #16) with current and wind conditions. (**c**) Numerical model of 10 hinged plates (#01, #02,. . ., #10) with current and wind conditions.

Table 1 provides a summary of the overall design specifications for both the floating structure with the individual plates and simulation parameters. Additionally, this implementation of a structure composed of interconnected plates aims to replicate the deflections of a long, horizontal flexible floating structure, as AQWA® primarily treats bodies as rigid and does not inherently accommodate this feature. Because of this, a value for the rotational stiffness of each joint about its x-axis must be determined so that the structure is satisfactorily rigid for the simulations.

Table 1. Details of structural specifications of the floating and individual plates with current and wind loads.

Parameters	Symbols	Ranges of Values
Total length (m)	L_f	69
Individual plate length (m)	l	3.355

Table 1. *Cont.*

Parameters	Symbols	Ranges of Values
Width (m)	b	5
Thickness (m)	d	0.4
Gap between plates (m)	G	0.1
Mass (t)	m	3250
Rotational stiffness (N.m/rad)	k_{rot}	4.00×10^6
Mooring stiffness (N/m)	k_f	10^3
Moments of Inertia (t.m^2)	m_i	I_{xx} = 552,787.5015 I_{yy} = 248,090.8140 I_{zz} = 792,211.3875
Wind speed (m/s)	U	0–5.0
Current speed (m/s)	V	0.5–2.0

2.2. Multi-Body Hydrodynamics

The numerical implementation employs a mathematical model that closely resembles the one introduced by [44]. It is considered that the wind is a constant speed of U and a steady current flow at a constant velocity $V = V{\cdot}\cos\theta$ along the path of wave flowing along the +ve x-axis. Assuming the water behaves ideally and applying the linearized wave theory, the velocity potential is expressed as $\Phi = \phi\, e^{-i\omega t}$, where ϕ represents the velocity potential that does not depend on time, ω (rad/s) represents the angular frequency, and t (s) is the time. Hence, ϕ is satisfied as follows:

$$\left(\frac{\partial^2}{\partial x^2} + \frac{\partial^2}{\partial y^2} + \frac{\partial^2}{\partial z^2}\right)\phi = 0 \text{ in } \Omega \tag{1}$$

$$\left(\frac{\partial}{\partial z} - K\right)\phi = 0, \text{ on } S_F \tag{2}$$

$$\frac{\partial \phi}{\partial n_k} - \vec{V}_{S_k}.\,\vec{n}_k = 0 \text{ on } S_k \tag{3}$$

$$\phi_z = 0 \tag{4}$$

$$\lim_{r\to\infty} \sqrt{r}\left(\frac{\partial}{\partial r} - iK\right)\phi_{R_k} = 0, \text{ on } S_\infty \tag{5}$$

where $K = \omega^2/g$. The fluid domain is denoted as Ω, S_F indicates the free surface, S_B refers to the water bottom, S_∞ is the limit at infinity, and the surface of the wetted plate is represented as S_k, where k varies from 1 to 20, corresponding to each plate.

The plates are linked by hinges that provide rotational stiffness, and the structure's edges are linked to mooring lines that have a certain level of stiffness k_f. The green circles designate the location of the centre of mass for each module, coincident with each local axis.

For the kth plate module, the unit vector $\vec{n}_k$ is *normal to* S_k and oriented outward, while $\vec{V}_{S_k}$ represents the fluid velocity at S_k. After determining the velocity potential ϕ, calculations for added mass and radiation damping can be performed. Then, ϕ can be represented as the total of the ϕ_I, ϕ_D, and ϕ_R

$$\phi = \phi_I + \phi_D + \phi_R \tag{6}$$

where ϕ_I represents the incident potential, ϕ_D denotes the diffraction potential, and ϕ_R refers to the radiation potential. Hence, the excitation forces, $F_{w_j}^{(k)}$, can be associated with ϕ_I and ϕ_D for the jth DOF and the kth mode through the following relationship:

$$F_{w_j}^{(k)} = \rho i\omega \iint_{\overline{S}_k} (\phi_I + \phi_D){\cdot}\vec{n}_k dS, \tag{7}$$

In this context, ϕ_I refers the incident potential, ϕ_D denotes the diffracted potential, ρ indicates the fluid's density, ω refers to the wave frequency, and $\overline{S}_k$ represents the average wetted surface area for each module k.

The generalised added mass [a] and radiation damping [b] can be expressed as follows:

$$[a] + \frac{i}{\omega}[b] = \rho \iint_{\overline{S}_k} \phi_R \cdot \vec{n}_k dS, \tag{8}$$

where $[a] = A_{jk}^{(mn)}$ and $[b] = B_{jk}^{(mn)}$ with the jth mode of the mth plate that is caused by the kth mode of the nth plate. Focusing on six DOFs and following the methodology of [9], in the frequency domain (FD), the motion equation for the free multimodule FFS is read as

$$[M + A(\omega)]\ddot{X} + B(\omega)\dot{X} + KX = F_W(\omega), \tag{9}$$

In this context, M refers to a mass matrix encompassing all bodies, where the diagonal entries consist of 6×6 mass matrices for each individual plate k. Similarly, the hydrostatic stiffness matrix K is established in a manner akin to the mass matrix, accommodating each plate's characteristics and its six DOFs. The added mass and radiation damping matrices, denoted as $A(\omega)$ and $B(\omega)$, refer to the added mass and radiation damping matrices, comprise $k \times k$ matrices, each made up of 6×6 blocks. The vector X indicates the displacement, which leads to its first derivative $\dot{X}$ and second derivative $\ddot{X}$ over time. Additionally, F_W (ω) is the vector of wave-induced forces exerted on all k bodies.

In the FD, after determining the hydrodynamic coefficients using AQWA to address the earlier outlined equations, the system can additionally be represented in the TD. The differential equations framework applied within the TD can be encapsulated by the Cummins equation:

$$(M + A_\infty)\ddot{x}(t) + (K + K_E)x(t) = f_W(t) + f_E(t) + f_C(t) \tag{10}$$

$$A_\infty = A(\omega) + \int_0^\infty R_f(t)\frac{\sin(\omega t)}{\omega}dt \tag{11}$$

$$f_C(t) = -\int_0^\infty R_f(\tau)\dot{x}(t-\tau)d\tau \tag{12}$$

$$R_f(t) = \frac{2}{\pi}\int_0^\infty B(\omega)\cos(\omega t)d\omega \tag{13}$$

$$f_w(t) = Re\left\{\sum_{j=1}^{N} A_{wj}L(\omega_j)e^{i(k_j x - \omega_j t - \alpha_j)}\right\} \tag{14}$$

After the hydrodynamic coefficients have been established, the structural mass matrix is symbolized as M, while the added mass matrix for the fluid is labeled A_∞. This equation also incorporates an additional stiffness matrix, K_E, which arises from the connections between the plates, $x(t)$, $\dot{x}(t)$, and $\ddot{x}(t)$ denote the displacement, velocity, and acceleration vector of the multibody floating structure, respectively. Wave excitation forces are denoted by $f_W(t)$, external forces from the mooring by $f_E(t)$, and convolution forces by $f_C(t)$. $R_f(t)$ is the retardation function matrix, that is Fourier cosine transform of $B(\omega)$; $L(\omega_j)$ is linear wave excitation at jth frequency; and α_j is the phase angle (for further details, see [10]).

It may be mentioned that AQWA integrates this system of equations over time by employing a two-stage predictor–corrector numerical method, and further details on its application are available in the Theory Manual [45].

3. Brief Description of Experiment

3.1. Experimental Model and Equipment Adopted

The experiments were carried out at the wave flume located within the National Laboratory for Civil Engineering (LNEC) in Portugal. A piston–flap wavemaker is positioned at one side of the flume to produce regular waves, while, at the other side, a rocky slope "beach" zone is created to strongly dissipate incoming wave energy, thereby minimizing reflection. The wave flume measures 35 m in length, 0.62 m in width, and 1 m in height while maintaining a constant water depth of 0.35 m (illustrated in Figure 2).

Two model tests were carried out in the mentioned wave flume to obtain two-dimensional locations of targets placed either on the free surface or on the interconnected structural model. The following is a brief description of the two apparatuses: targets, a supporting frame, and a model.

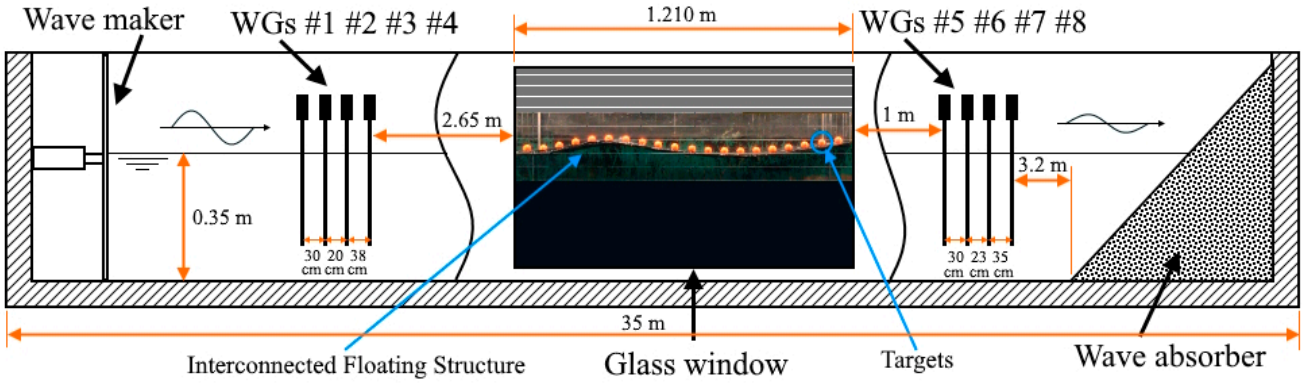


Figure 2. Detailed illustration of the wave flume showing the interconnected plates, arrangement of tracking targets, and WGs (#1, #2, #3, #4, #5, #6, #7, #8).

The free surface elevation within the wave flume is monitored using eight WGs (wave gauges), with the voltage alerts obtained via a NI-9205 module from National Instruments and transmitted to a PC at a frequency of forty Hz. The WG distances are provided in Table 2.

Table 2. Distance between WGs.

WGs	Unit	Distances
#1 and #2	cm	30
#2 and #3	cm	20
#3 and #4	cm	38
#5 and #6	cm	30
#6 and #7	cm	23
#7 and #8	cm	35
#4 positioned in front of #5	m	4.65
#8 positioned before the front edge of the rock	m	3.2

Situated between the two groups of WGs is an area designated for model installation. This space features a glass window, allowing for visual assessment of the response during the experiment, and, in the context of the present study, a digital camera will capture the footage at 60 frames per second (fps). The camera is aligned at a right angle to the window glass, ensuring the model is centred in the frame. It is placed at a distance that reduces distortion and at a height where the camera lens's centre is level with the water surface in the flume.

3.2. Model Preparation and Wave Characteristics

The floating interconnected system consists of 20 wooden panels coated with silicone and interlaced with EVA (Ethylene Vinyl Acetate), which serve as hinges and restrict their rotational movements based on the plates' thickness. Each panel is 7 mm in height, 59 mm in width, and 526 mm in length, with an average mass of m = 0.119 kg.

The model depicted in Figure 3 (showing a top view of the 20 hinged plates in a wave tank) is designed to exhibit geometric, Froude, and Cauchy similarities with the 1:57 scale model [46]. To attain elastic similarity, flexible EVA was selected as an appropriate material due to its elastic modulus (about $E = 3 \times 10^7$ N/m^2), which effectively mimics the actual scale articulations.

The model is secured using two stainless-steel frames, each equipped with five reinforced steel wires to protect drifting. These cables extend vertically along the frames, with each one threading through steel rings that are fastened to both the front and rear ends of the interconnected floating structure model, as illustrated in Figure 3. The frames are equipped with steel plates on top to allow for weight to be applied to them, which secures both the frames and the weight in position atop the flume and inhibits horizontal movement. This experiment primarily investigates the vertical movement of floating articulated plates across various time intervals. The front of the model is 2.65 m away from WG #4.

In the current experiment, incident waves are assumed to be regular waves, and the wave features of the wave height vary between 40 mm, 60 mm, and 80 mm, while the wave period spans from 0.8 s to 3.0 s, increasing in increments of 0.2 s.



Figure 3. Floating interconnected structure with targets inside the wave flume.

3.3. Technique for Tracking Targets

Using Python 3.9, the algorithms for tracking and identification in video frame image processing have been developed based on the OpenCV 4.5.0 library. Every test's video is analysed by evaluating each frame as an individual image (Figure 4). In every one of those frames, predetermined areas are chosen for tracking by the algorithm, and within these areas (represented by blue rectangles), the target is located by filtering the image's colours.

This filtering process can isolate specific areas of the image that fall within a selected range of shades of a particular colour, like the orange selected for the targeted elements.

Following this technique, only the section showcasing a spectrum of colours, including the target, remains. The picture is subsequently transformed into grayscale, allowing the Hough Circle Transform to be utilised for the area of interest within the monochromatic frame using defined parameters, including a range of radius values for the algorithm to search. The final step provides the horizontal and vertical coordinates of the centre of the detected circle (represented by the magenta circles). As the target is secured to the structure, the movement accomplished by a particular tracked target is mirrored by the corresponding plate, therefore resulting in the vertical movement of each module of the current model.

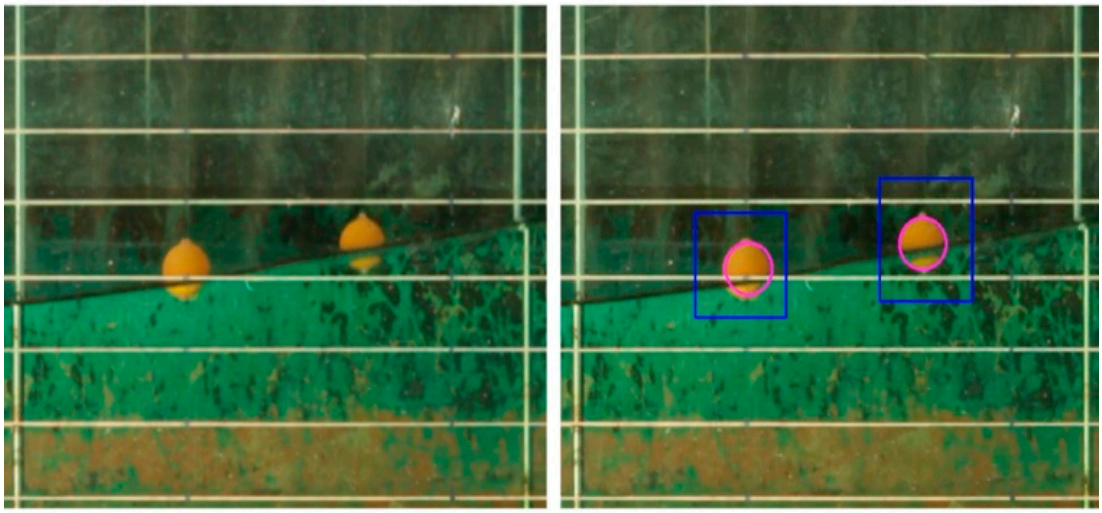


Figure 4. Floating tracking targets (tracked box (blue) and the circle (magenta) indicate the identified target) can move vertically when the waves pass.

The tests are carried out to analyse the motions of floating interconnected plates that emulate a flexible structure, an important feature for structural analysis in engineering applications in the marine environment.

4. Quantitative Findings and Analysis

This section compares the displacements from the current numerical simulations with experimental data from [34] and analysis of structural responses for various current speeds and wind loads, which did not account for the current and mooring lines. Here, the results for the opposite current case are avoided as they are not considered in the formulations due to the case of wave blocking.

The model originated for the numerical process and was divided into a mesh with a local element size of 0.2 m and a defeaturing tolerance of 0.05 m, resulting in a total of 22,040 elements, of which 10,180 were diffracting panels. The hydrodynamic response modules were configured in the time-domain simulations to address the problem using a time step of t = 0.01 s.

Numerical simulations utilizing ANSYS AQWA are conducted on an 8-core Intel® i7 CPU (Intel (American multinational corporation and technology, Santa Clara, CA, USA)) running at 3.6 GHz, equipped with 16 GB of RAM. Under this configuration, addressing the problem in the FD requires approximately 4–5 h to determine the hydrodynamic coefficients for 26 wave frequencies, with a 60-degree interval between the waves. Additionally, an extra hour is required to execute the simulations in the TD, resulting in approximately 5 h of results for hydrodynamic response.

The parameters established for wave generation are obtained from the measurements, and the results are compared in Table 3, where the relative errors of the parameters of the wave, H and T, are shown. The wave height recorded using the target tracking method is consistently greater than the measurements obtained from the WG, which also exhibits some degree of value overestimation. Conversely, positive outcomes were observed when analyzing the wave period, likely because the measurements taken with the targets were smoother compared to the wave gauge, which produces a noisier signal.

Table 3. Different test cases of measurements of wave height (H) and wave period (T) obtained using the target tracking technique and the traditional WG method.

Parameter	% H Difference			% T Difference		
Case	**Target #1**	**Target #2**	**WG #4**	**Target #1**	**Target #2**	**WG #4**
H = 4; T = 1	8.1%	8.8%	6.8%	0.4%	0.4%	1.5%
H = 4; T = 3	4.4%	6.0%	4.2%	1.1%	1.1%	0.4%
H = 8; T = 1	13.7%	13.7%	10.2%	0.4%	0.4%	1.5%
H = 8; T = 3	12.7%	6.8%	3.9%	1.1%	1.1%	0.4%

The target tracking method appears to show a propensity for delivering more accurate wave height estimates for longer wave periods, but this comes at the expense of diminished accuracy in the wave period estimation. This trade-off in estimating wave height and period is evident as the relative error in period measurements decreases when the corresponding wave height estimates show a greater disparity. Based on this information, it can be inferred that a longer wave period results in more accurate estimations of wave height, suggesting that more powerful waves provide improved measurements.

4.1. Results and Analysis of the Comparison

In this subsection, the present numerical simulations of displacements and wave quantities are compared against model numerical and analytical test results with no current and mooring lines [34] versus wave period, nondimensional structural length, and nondimensional wavelength to check the level of accuracy.

Figure 5 shows the comparison results between the present numerical and experimental data sets [34], where the vertical displacements of the fifth plate (ξ_3), expressed as a ratio to the wave amplitude (A_w), are analysed for the interconnected structure model with a height of $H = 3.42$ m versus time (s). It can be observed that in the numerical result, the vertical displacement is smaller at the crest due to the presence of hinges and mooring lines with certain values of stiffness attached to the 1st and 20th plates, which indicates that choosing proper stiffness for mooring lines can enhance the structural stability of the system by limiting the structural displacement. Additionally, as shown in Figure 5, the current numerical model shows a displacement of 0.93 m, whereas the displacement from experiment measures 1.2 m, which is 22.5% lower.

Figure 6 compares the current numerical and experimental results for the vertical displacement (considered at the point mass of each plate) of the interconnected structure normalized by the wave amplitude of the structure model across the normalized structural length (x/L). The overall trend of both numerical and experimental results is similar; nonetheless, there are certain distinctions between the two outcomes, particularly for the first plates in the numerical analysis in which the result shows higher displacement than the experiment with an overall relative difference $\Delta = 1\% - 20\%$ between the numerical result and the experiment result in vertical displacement. Moreover, in Figure 6, the maximum displacement difference is noticed at the first plate, where the displacement

from the experiment is 0.93 m, while the numerical model is observed at 1.16 m, which is 19.83% lower.

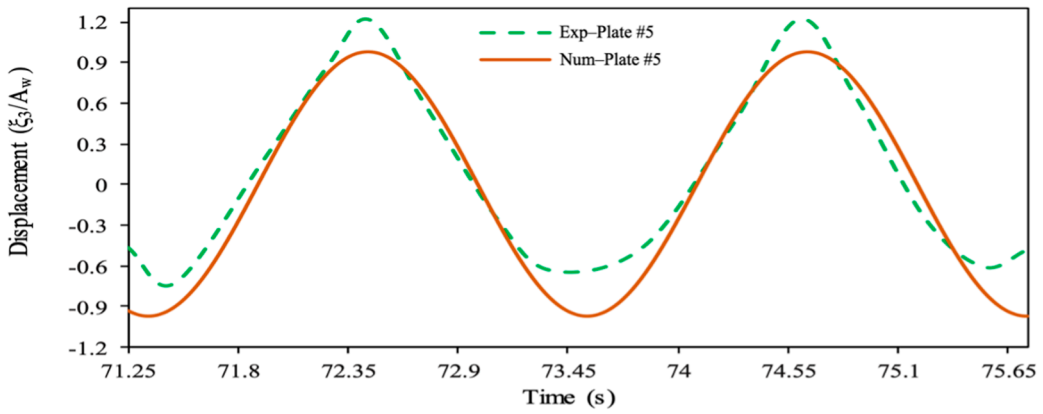


Figure 5. Comparison between numerical simulation and experimental data sets [34] of the structural vertical displacement for 5th plate versus time with $A = 1.7$ m and $T = 4.2$ s.

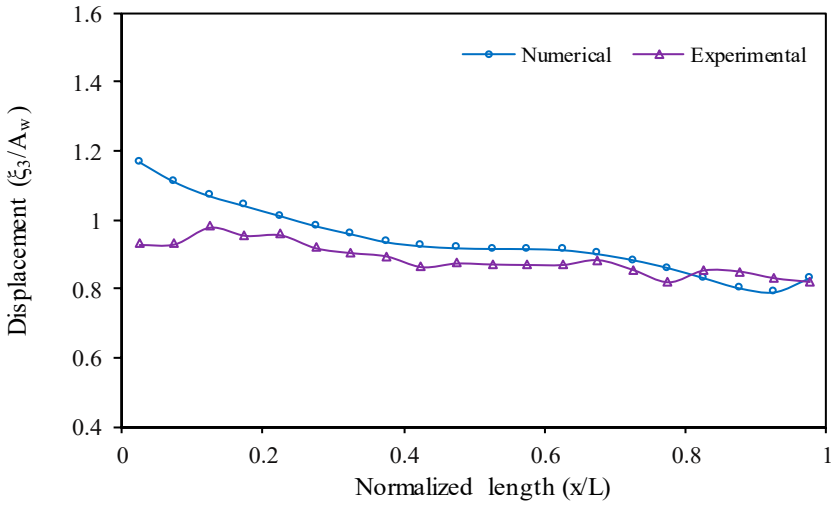


Figure 6. Comparison between the numerical and experimental data sets [34] of the structural vertical displacement with $A = 1.7$ m and $T = 4.6$ s for the floating interconnected structure.

Figure 7 shows the comparison between (a) the reflection coefficient K_r and (b) the transmission coefficient K_t (for calculation, see Section 4.3) computed by the present numerical simulations and the analytical model results from [44] versus non-dimensional wavelength λ/L for $k_f = 10^6$ N/m for a small value of the current speed $V = 0.5$ m/s, along with other parametric values, which are the same as mentioned in Table 1. Figure 7 demonstrates that in the trend of K_r and K_t, the values are alike and very close for both, indicating that the two model results align well.

In Figure 7a, when $\lambda/L \leq 2$ and for the intermediate value of λ/L, the numerical result K_r converged to the numerical and analytical model, whilst K_r values are close for some data points. However, at a specific λ/L, a discrepancy arises between them. The reason for this is that the existing speed in the upstream area transmits more wave energy that flows over the interconnected and underlying structures, resulting in reduced reflection in the current model. This effect is not observed in the predicted models [44]. Consequently, the present numerical model exhibits a bit higher reflection coefficient compared to the findings of the analytical and numerical models [44].

On the other hand, in Figure 7b, for smaller and higher values of λ/L, the present numerical result K_t converged, but for intermediate values of λ/L, the data points are very

close to the numerical and analytical results and the reasons are reverse to that of K_r. In addition, the results observed in the case of K_t are similar to that of [47] when the wave interacts with a floating moored flexible membrane without current conditions.

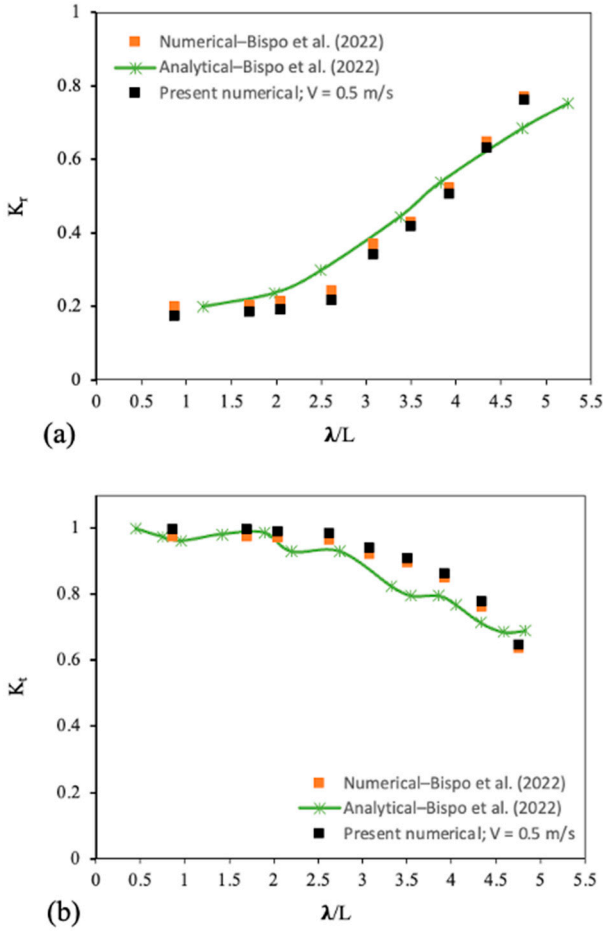


Figure 7. Comparison of (**a**) K_r and (**b**) K_t with numerical and analytical results [44].

Furthermore, the difference observed, 8.69%, for K_r is close to $\lambda/L = 2.6$, where the present numerical model is 0.23, while the numerical model from [44] is 0.25. Conversely, for K_t, near $\lambda/L = 2.6$, the present numerical result is 0.89, whilst the numerical simulation and analytical result from [44] are 0.88 and 0.85, with the difference being 1.12% and 4.49%, respectively. It may be highlighted that the comparison between K_r and K_t shows (Figure 7) that the numerical and analytical results from [44] are more accurate than the data presented in Figures 5 and 6.

Figure 8 shows a comparison result between the RAO of vertical displacement amplitude of the interconnected structure versus normalized length under different arrangements (see Table 4) with a certain value of wavelength, $\lambda = 90$ m, subjected to current load with a constant speed of 0.5 m/s. The comparison reveals that the whole system becomes more stable as the number of bodies used in the model and accordingly the total length of the interconnected structure increases. This is likely due to the increased structural integrity, which causes a reduction in the vertical displacement result. Furthermore, the maximum displacement is observed at the first body in all three cases, where in case #3 the displacement is 1.085 m, while the present model is observed at 0.998 m, which is 8.72% higher.

Table 4. Comparison cases for different arrangements (other design parameters for cases #2 and #3 are the same as in Table 1).

Case Numerical	Arrangement	Length
Case #1	Present model (20 bodies)	69 m
Case #2	16 bodies	55.18 m
Case #3	10 bodies	34.45 m

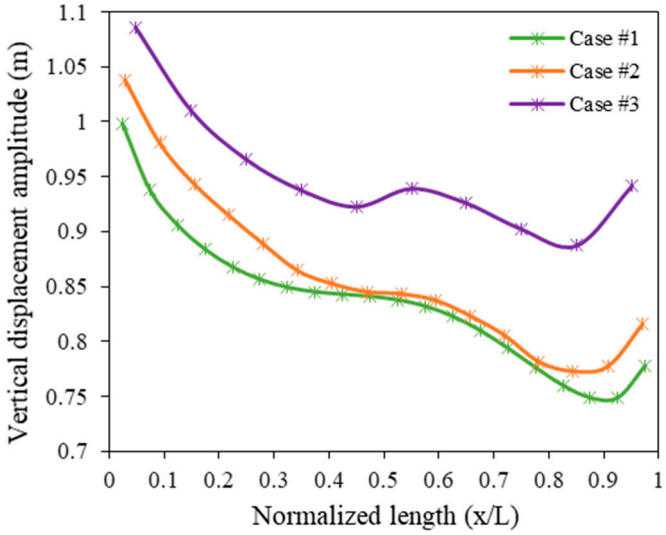


Figure 8. RAO of vertical response for different arrangements with current speed of V = 0.5 m/s.

4.2. Impact of Current and Wind Loads on the Vertical Displacements

It is presumed that a steady current is moving at a velocity $V = V \cdot \cos\theta$ during wave propagation along the +ve x-axis.

Table 5 presents the numerical data (sourced from AQWA) regarding the vertical displacements of individual modules under various wind loads while maintaining $v = 2$ m/s. The impact of U on the structural displacement is minimal across the different wind loads. It is important to highlight that in AQWA [45], the drag force of the wind is computed based on the U at a height of 10 m above the reference point above the waterline. Additionally, the U near the still water line (SWL) is quite limited in size; this indicates that the wind loads on the floating foundation near the SWL can be regarded as insignificant [17].

Table 5. Maximum displacement (m) under various wind loads (U) with constant current speed, V = 2 m/s.

U	η_1	η_2	η_3	η_4	η_5	η_6	η_7	η_8	η_9	η_{10}	η_{11}	η_{12}	η_{13}	η_{14}	η_{15}	η_{16}	η_{17}	η_{18}	η_{19}	η_{20}
0 m/s	0.983	0.959	0.944	0.936	0.931	0.928	0.925	0.921	0.916	0.910	0.902	0.893	0.883	0.871	0.860	0.850	0.842	0.839	0.843	0.865
3 m/s	0.983	0.959	0.944	0.936	0.931	0.928	0.925	0.921	0.916	0.910	0.902	0.893	0.883	0.871	0.860	0.850	0.842	0.839	0.843	0.865
5 m/s	0.983	0.959	0.944	0.936	0.931	0.928	0.925	0.921	0.916	0.910	0.902	0.893	0.883	0.871	0.860	0.850	0.842	0.839	0.843	0.865

The results presented in Table 5 demonstrate that the vertical displacement remains unchanged in the case of different wind loads, indicating that wind has no impact on the floating interconnected structure.

Figure 9 demonstrates that as the length increases from plate #1 to plate #20, the vertical displacement amplitude generally decreases in all three cases (V = 0, 0.5, 2 m/s). However, the rate of decrease changes depending on the current speed. The result representing the highest current speed (V = 2 m/s) shows the highest vertical displacement amplitude with increasing length. As currents exert hydrodynamic forces on the floating

interconnected structure, results in a higher displacement with certain values of mooring and rotational stiffness.

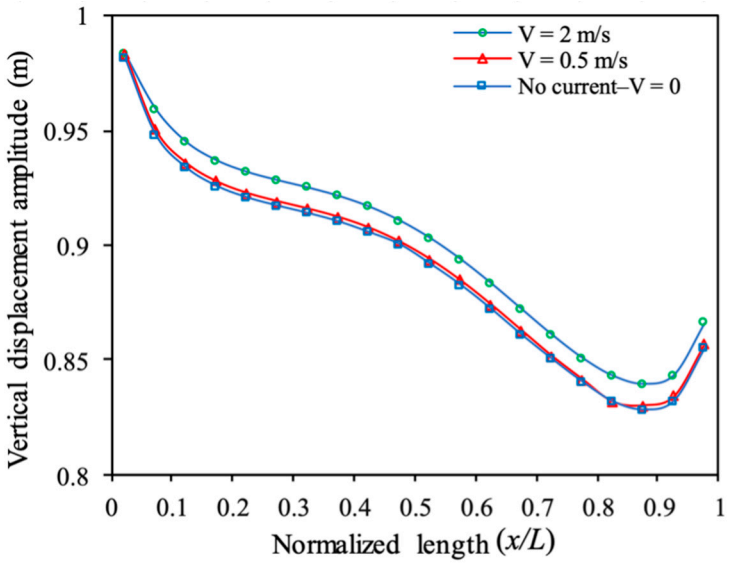


Figure 9. RAO of vertical response for different V with a certain value of wavelength of $\lambda = 120$ m.

In Figure 10, the general trend is that the displacement amplitude diminishes for shorter wavelengths as the length rises with the steepest slope than for longer wavelengths. However, the maximum vertical displacement occurred for shorter wavelengths at plate #1. Meanwhile, the minimum vertical displacement was also observed for shorter wavelengths at plate #19. This suggests that the floating interconnected structure is more prone to deflection at higher frequencies; as a result, most of the wave energy induced by shorter wavelengths is captured by plate #1, and reduced wave energy leads to decreased hydrodynamic forces acting along the whole structure.

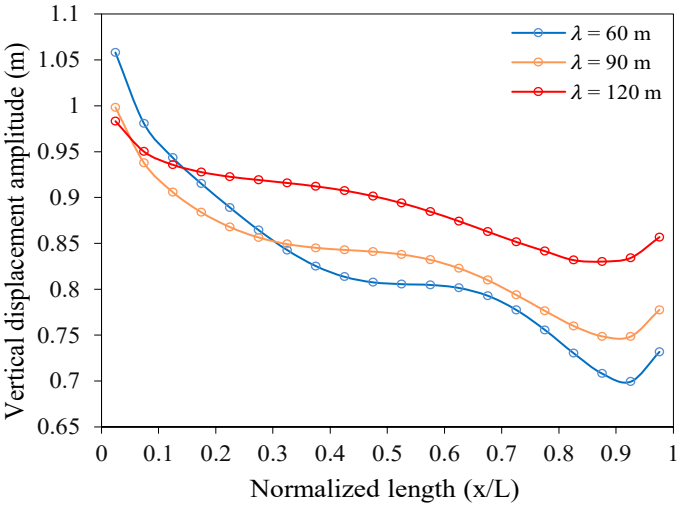


Figure 10. RAO of vertical response for different λ values with constant current speed of $V = 0.5$ m/s.

Figure 11 shows that as the length increases, the vertical displacement amplitude decreases and then increases for the last three plates (Plate #17 to #20) in the presence of different wave and current directions. Also, the wave and current direction positively impact the vertical displacement amplitude, particularly at angles of attack between 30° and 60°. Increasing the wave–current direction leads to greater vertical displacement, especially at the middle and last plates, while this is in reverse for the first and second plates. This

occurs because when the angle of attack is perpendicular to the floating interconnected structure, the wave force travels along the floating horizontal plate in the x-direction. It can also be stated that since the wave–current direction is at a lower angle, the first plate encounters the wave and has the bigger displacement, and this displacement will dissipate along the other plates when compared to plates #1 and #2. This can be explained by the fact that plate #1 is the first plate connected to the structure and will react not only to the wave but also to the tension in the cable.

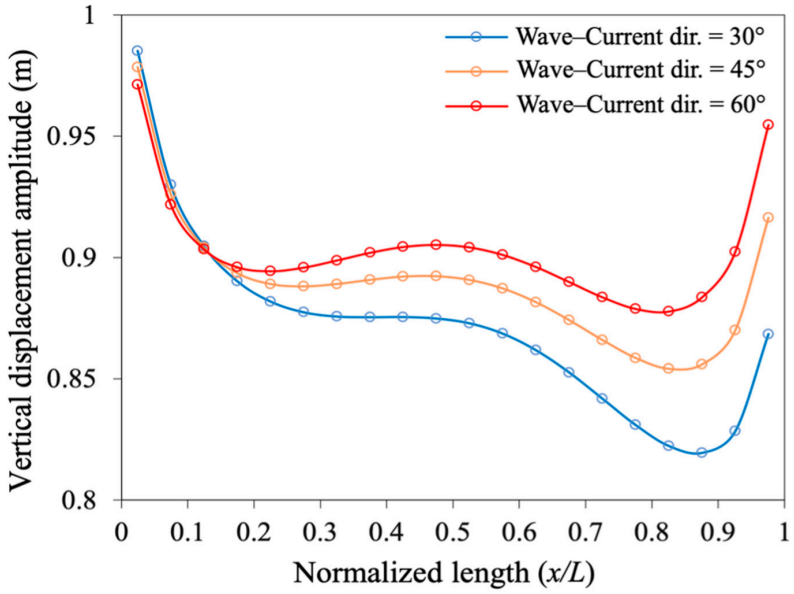


Figure 11. RAO of vertical response for different wave–current directions with constant current speed of 0.5 m/s and a specific value of wavelength of $\lambda = 90$ m.

Figure 12 shows the force exerted on two mooring lines (mooring lines #1 and #4) over time. The rapid fluctuation in force on mooring line #1 suggests that it experiences a higher dynamic load than mooring line #4; this could be due to the location of mooring line #1, which is located at fore of the structure attached to the 1st plate rather than mooring line #4 connected to the 20th plate, which experiences less dynamic load and hence less tension in the mooring lines.

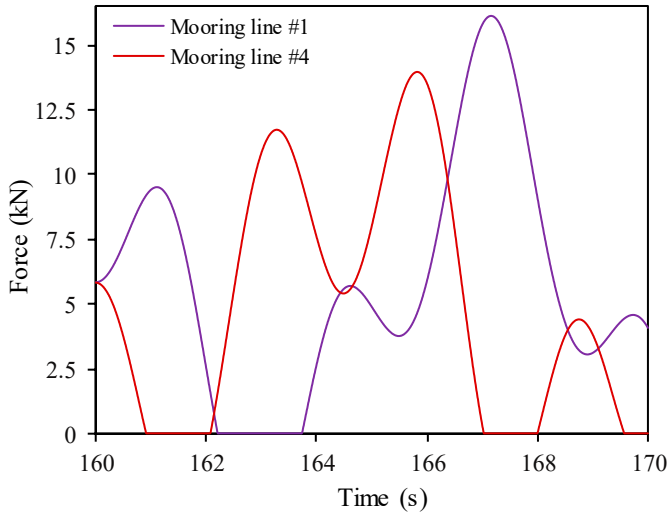


Figure 12. Time series data of the tension exerted on the mooring lines at both the front and rear of the model with $V = 0.5$ m/s and wave–current direction of 0°.

Figure 13 gives the RAO of the heave response of floating interconnected structure for different rotational stiffness with a current speed of V = 0.5 m/s versus normalized structural length. It is found that increased rotational stiffness results in reduced vertical displacement across the whole length of the structure since higher rotational stiffness results in greater rigidity and reduced vertical displacement. Furthermore, a higher rotational stiffness indicates that the floating interconnected structure exhibits greater resistance to rotation around its local x-axis at the joints, making it less susceptible to vertical displacement, ultimately contributing to enhanced overall structural stability.

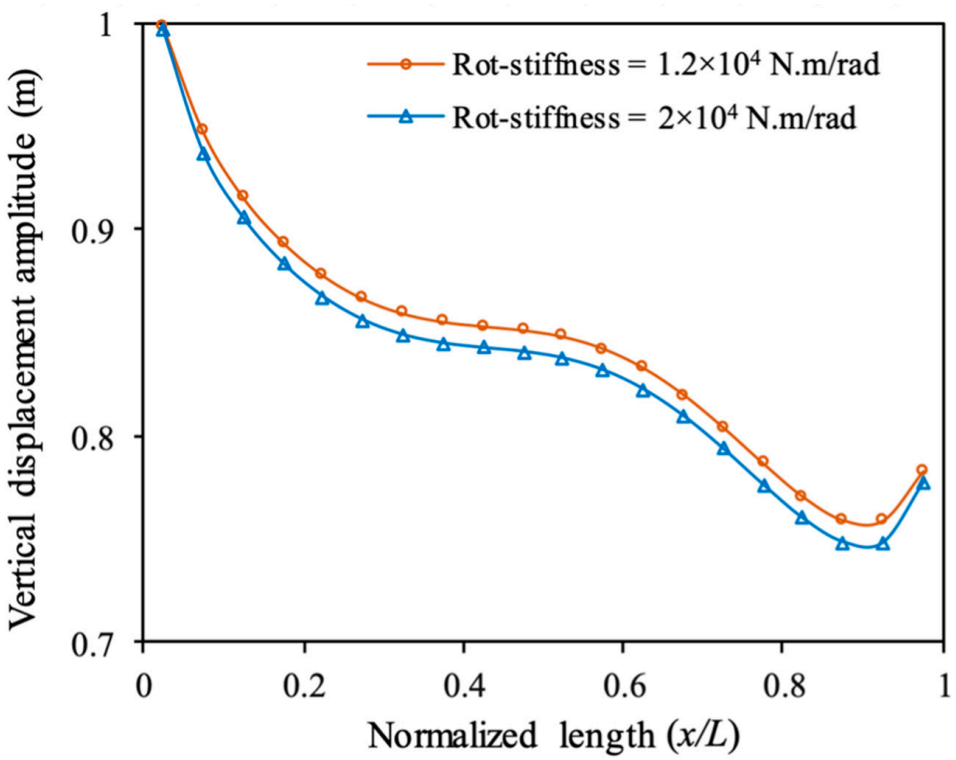


Figure 13. RAO of vertical response for different rotational stiffness with constant current speed of 0.5 m/s and a certain value of wavelength of λ = 90 m.

In the context of regular waves, Figure 14 displays the contours of wave elevation amplitude, normalized against the incident wave amplitude, with A_w set to 1 m. The shape of the amplitude located at the back of the structure shows the transmitted waves. The transmission coefficients tend to rise as the wavelength ranges from 90 m to 120 m. An increase in wave energy transmission below the floating interconnected structure leads to a decrease in the reflection coefficient at the forefront of the structure, as can be seen in Figure 14.

The contours of wave elevation amplitude at the front of the floating structure display the reflected wave. Furthermore, assuming that there is no energy loss during the reflection–transmission process, the transmission coefficient rises behind the floating structure due to an increase in wave energy transmitted beneath it. Consequently, it can be anticipated that the reflection coefficient decreases at the forefront of the structure.

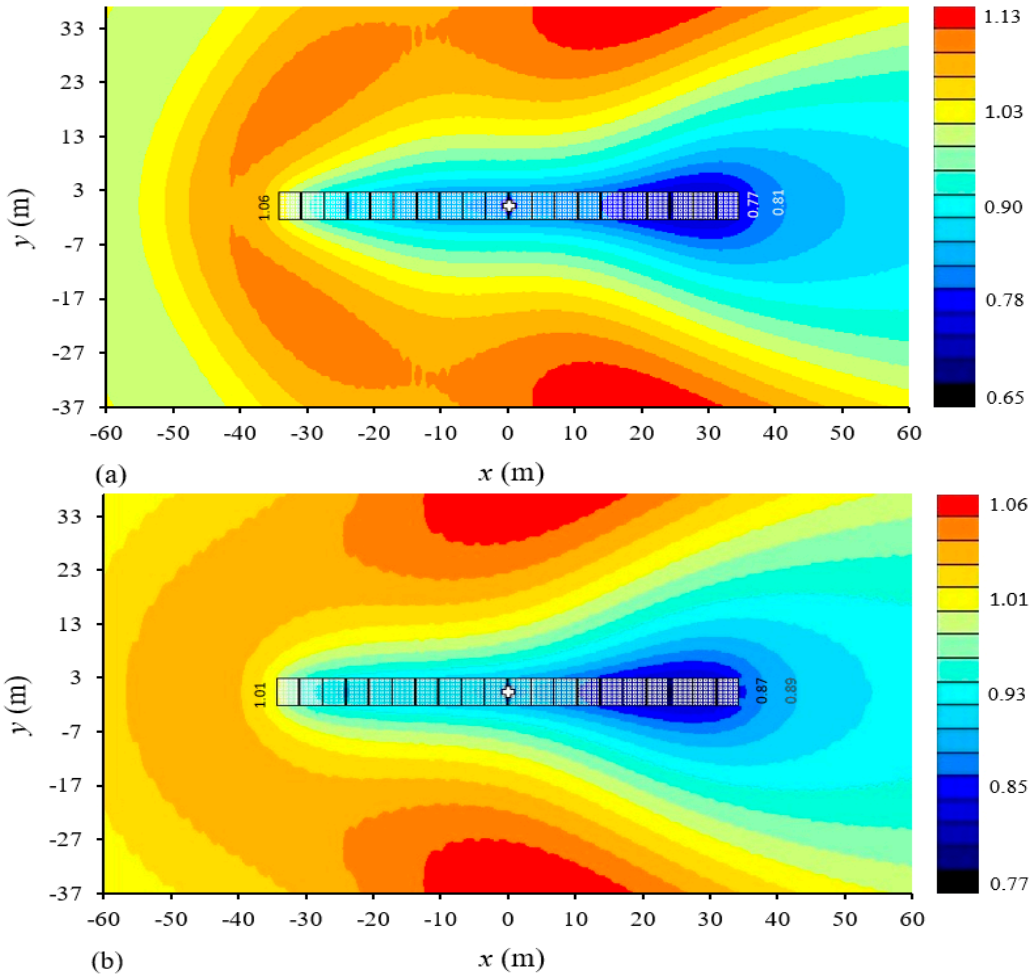
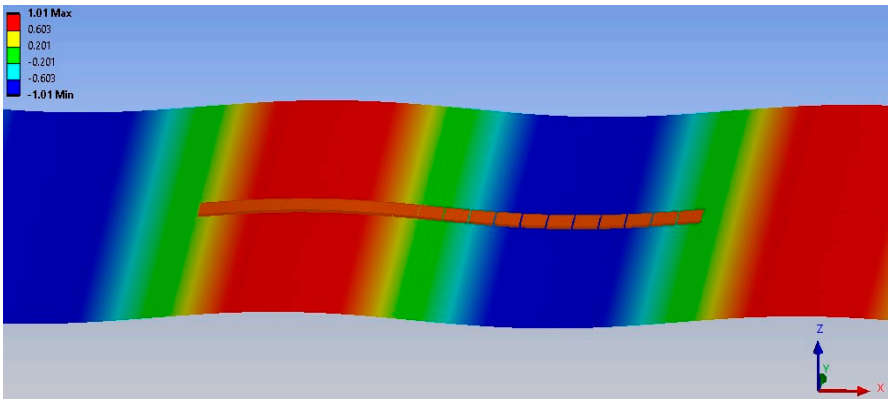


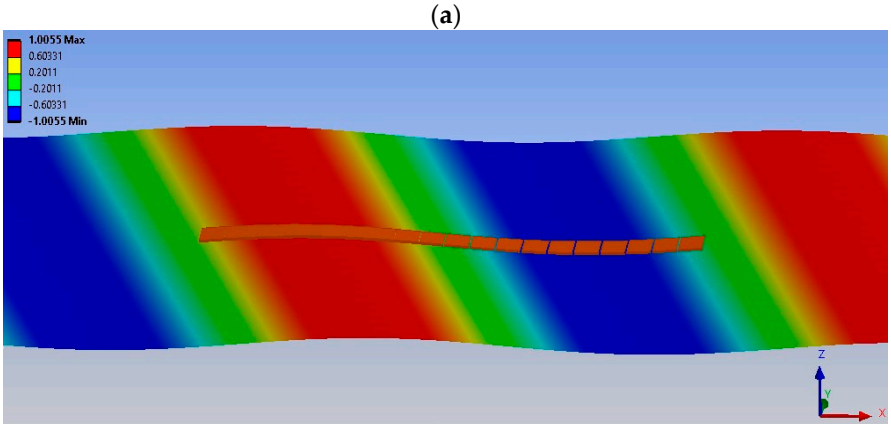
Figure 14. Contours for wave transmission around the interconnected floating structure with θ = 0.0 deg., A_w = 1 m: (**a**) λ = 90 m and (**b**) λ = 120 m.

Figure 15 represents the pressure and motion results obtained for different wave directions in the hydrodynamics diffraction regime. In Figure 15, the pressure and motion results obtained for different wave directions with wave frequency $\omega = 0.89$ rad/s are displayed in the hydrodynamics diffraction regime. It is noticed that as wave direction increases (from 0° to 60°), the floating structure experiences slightly less wave motion across the whole system (Figure 15a–e). This reduction can be attributed to the increased diffraction and more effective distribution and dissipation of wave energy within the floating structure with an increase in the angle of attack.

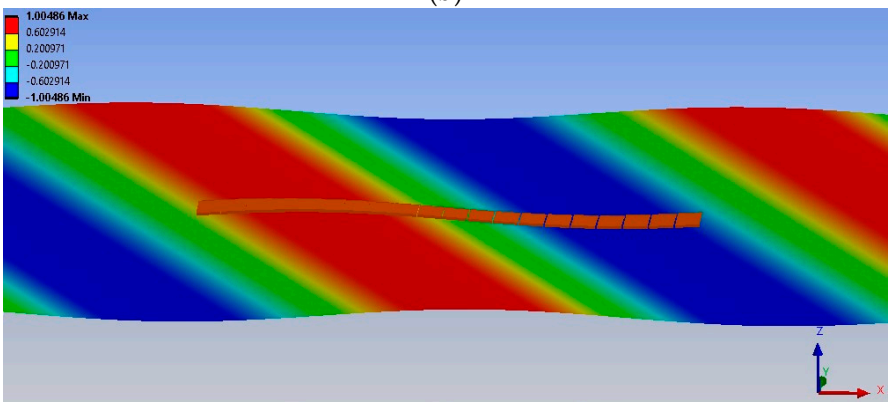
It may be mentioned that in the hydrodynamic response analysis, the consideration of opposing wave–current conditions is avoided because wave-blocking phenomena are occurring.



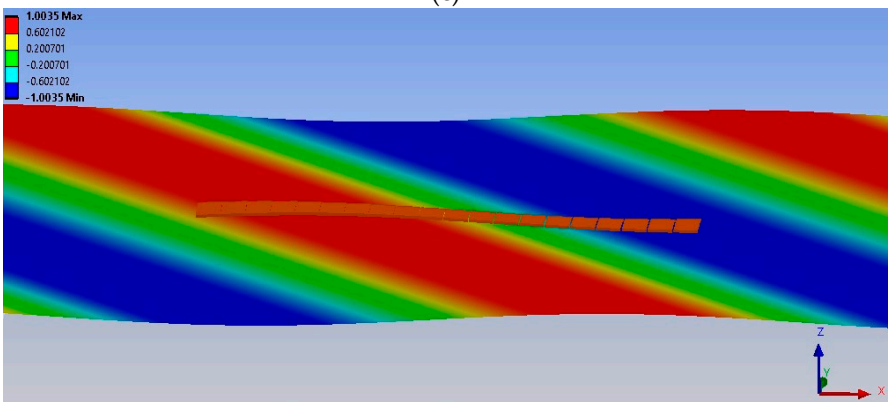
(**a**)



(**b**)

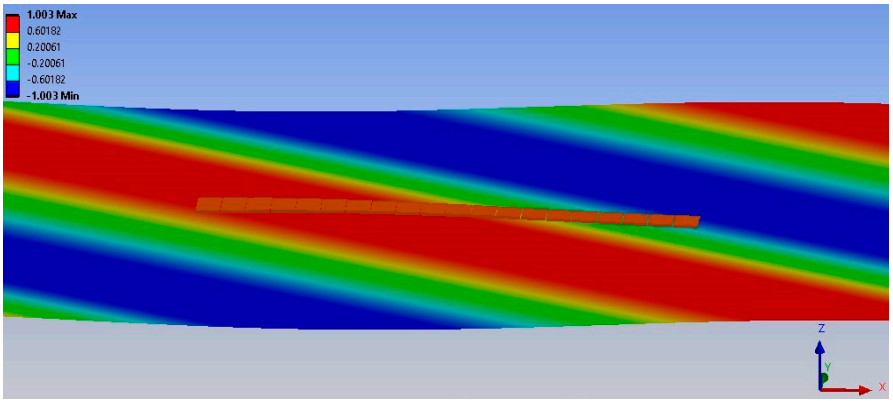


(**c**)



(**d**)

Figure 15. *Cont.*



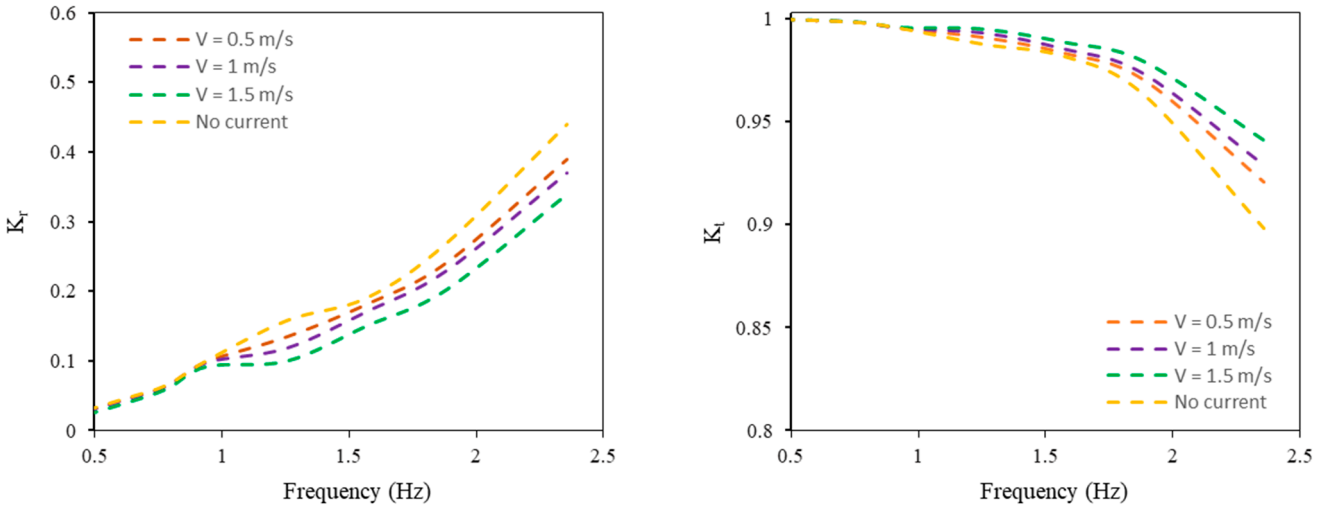
(**e**)

Figure 15. Hydrodynamic diffraction for floating interconnected structure $A_w = 1$ m for a certain value of wave frequency of $\omega = 0.89$ rad/s. (**a**) $\theta = 0°$ (**b**) $\theta = 15°$ (**c**) $\theta = 30°$ (**d**) $\theta = 45°$ (**e**) $\theta = 60°$.

4.3. Effect of Current Speed on the Reflection Coefficient K_r and Transmission Coefficient K_t

Using the method outlined [48], we can determine the reflection and transmission coefficients by measuring the envelope of the combined wave system created by the incident and reflected waves on the windward side of the structure, under the assumption that no energy is lost during the reflection–transmission process [48]. The coefficients can be calculated using the following formulas: $K_r = H_r/H_i$ and $K_r^2 + K_t^2 = 1$, where H_r and H_i denote the reflected and incident wave height determined by the vertical displacement of the wave. Therefore, the following results associated with K_r and K_t are computed under the influence of current and analyzed in detail.

Figure 16 demonstrates the impact of different current speeds V on (a) reflection coefficient (K_r) and (b) transmission coefficient (K_t) vs. frequency (Hz). It has been noted that the value of K_r diminishes for higher values of V, and with a rise in current speed, a significant amount of wave energy passes under the interconnected floating flexible structure, leading to a decrease in K_r. Further, for decreased values of frequency < 1, the differences in K_r for different currents are not significant, whilst this effect is remarkable for frequency > 1, and with varying currents, the trend of the transmission coefficient shown in (b) is reverse to that of K_r (as in [49,50]), showing a physically plausible energy balance equation that includes all values within the range of 1.0.



(**a**) (**b**)

Figure 16. Effect of current speed on (**a**) K_r and (**b**) K_t along with no current speed for $k_f = 10^6$ N/m.

Figure 17 shows the effect of mooring stiffness k_f on K_r and K_t with no current case vs. frequency (Hz) for current speed $V = 0.5$ m/s. It has been noted that for lower values of frequency (Hz), there is a negligible difference in the impact of mooring stiffness among K_r and K_t. However, for frequency (Hz) > 1.6, as the mooring stiffness increases, the reflection coefficient K_r increases, whilst this effect is reversed in the case of K_t. It can be explained that the floating flexible interconnected structure becomes rigid as the stiffness becomes higher, which leads to more reflection in the upstream region. The observations are similar to [44] without current speed. Further, it is noted that for all values of k_f, K_r and K_t present a physically realistic energy balance equation that is incorporated within the range of 1.0.

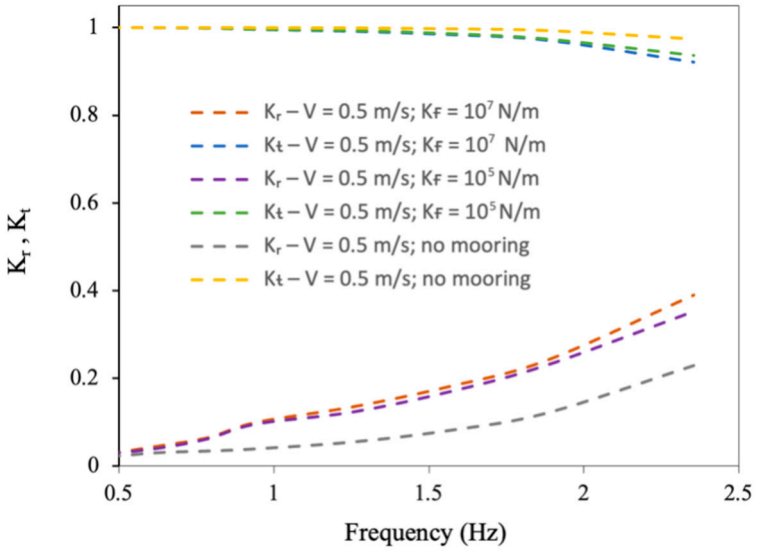


Figure 17. Effect of mooring stiffness on K_r and K_t.

Figure 18 compares the influence of h on K_r and K_t vs. frequency (Hz) with current speed $V = 0.5$ m/s. It shows that K_r diminishes as the depth of water rises and the observation of K_t is reverse to that of K_r. This occurs because an increase in water depth allows for greater transmission of wave energy underneath the large floating interconnected flexible structure, resulting in a reduction in the reflection coefficient K_r in the upstream region and heightened K_t in the downstream region; this is physically justifiable.

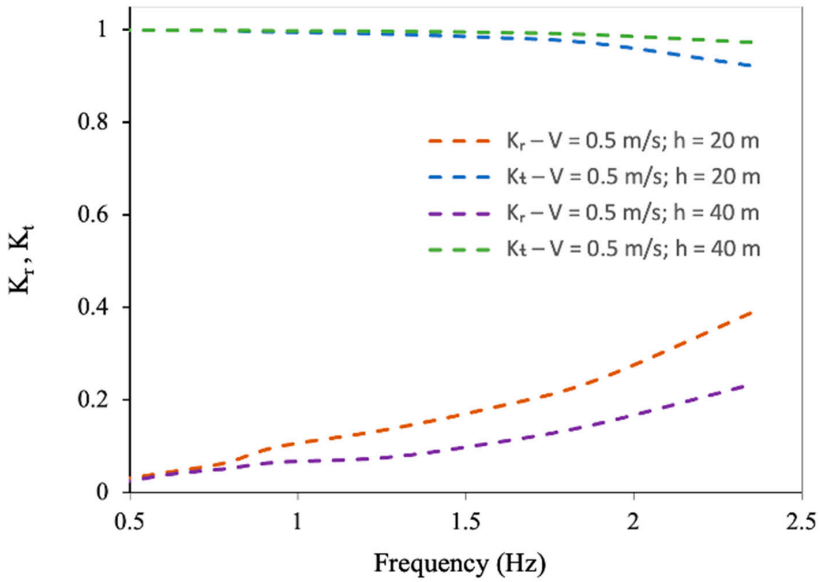


Figure 18. Influence of water depth on the K_r and K_t with current speed $V = 0.5$ m/s..

Figure 19 simulates the impact of rotational stiffness on K_r and K_t with current speed $V = 0.5$ m/s vs. frequency (Hz). It is seen that the value of K_r increases with an increase in the values of K_{rot}, whilst the observation is to be reversed in the case of K_t to that of K_r.

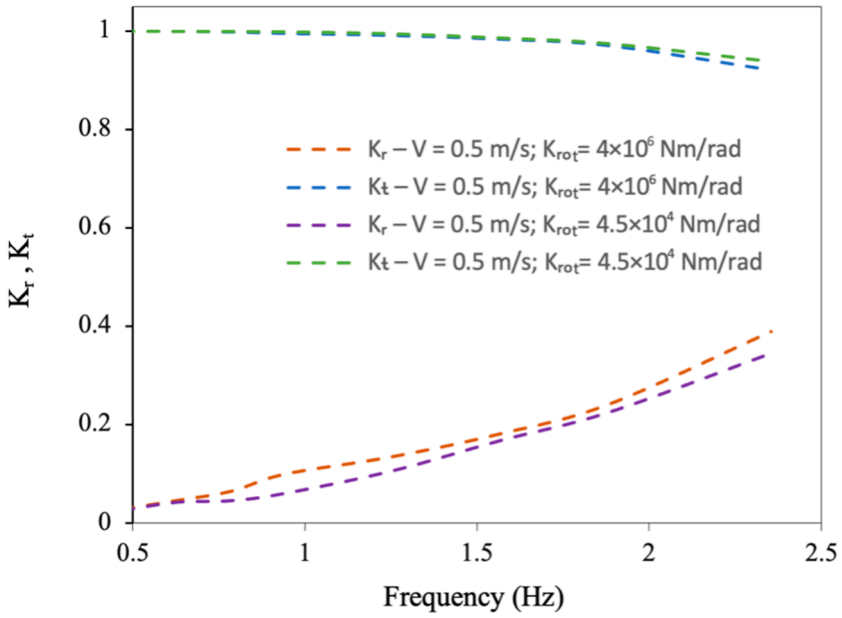


Figure 19. Effect of rotational stiffness k_{rot} on K_r and K_t with current speed $V = 0.5$ m/s.

5. Conclusions

The current study differs from the work in [44] in several key aspects: it incorporates an analysis of the impacts of current and wind on the hydrodynamic response of interconnected structures, includes comparisons with experimental data sets along with numerical and analytical results, evaluates new numerical models featuring 10 and 16 hinged plate bodies, examines wave transmission around the structure through contour plots, conducts hydrodynamic analysis at various angles of attack, and introduces a new section that investigates how currents, in conjunction with design parameters, affect reflection and transmission coefficients. The following remarks can be summarized.

For the first time, the comparison results between the numerically based BEM code and experimental data are presented for 20 bodies interconnected with hinges. Further, at a specific current velocity, a notable level of accuracy has been observed, suggesting that as the wavelength increases, the reflection coefficient decreases, while the transmission coefficient increases. A new analysis also examines the impact of environmental parameters like currents and winds on the hydrodynamic response to the present numerical model.

The maximum current speed signifies that the vertical displacement amplitude increases as the length grows. On the other hand, the overall patterns indicate that the amplitude of vertical displacement diminishes as the length increases, and for shorter wavelengths, it declines throughout the entire structure.

There is no observed impact of wind on vertical displacement; the wind drag force is calculated based on the wind speed recorded at a reference height of 10 m above the surface of the water, and hence, the wind loads on the floating structure near the SWL can be considered negligible.

The wave transmission typically rises as the wavelength extends from 90 m to 120 m. Conversely, it is important to highlight that the reflection coefficients decline as the wavelength increases at the front of the structure. Additionally, it has been noted that when the wave direction changes from 0° to 60°, the interconnected floating structure undergoes a minor decrease in wave motion across the entire system.

It is observed that as the current speed increases, the values of K_r become lower, which is due to a significant amount of wave energy passing under the interconnected floating flexible structure, whilst the K_t observations are just a reverse trend to that of K_r, showing a physically plausible energy balance equation that includes all values within the range of 1.0.

The current analysis can give us a better understanding of the impact of environmental parameters, potentially enhancing the serviceability, reliability, and safety assessments of marine operations for developing a large articulated floating flexible structure to design marine structure applications for offshore aquaculture bases, floating solar power plant bases, and wave energy conversion (WEC) platforms, creating multi-use platforms that can generate multiple forms of renewable energy.

The current numerical model in the AQWA software is limited to modelling a maximum of 20 structures. One more constraint is that for the current numerical model implemented with narrow gaps, near-field hydrodynamic interactions can be significant and AQWA may not always capture these interactions with sufficient accuracy, potentially leading to inaccurate predictions of motions and loads, especially under resonance conditions with green water. Therefore, assessing the hydrodynamic performance of these configurations under extreme sea conditions or large motions where nonlinear effects become significant would require a fully nonlinear potential-flow solver or more sophisticated techniques.

Concerning the experiment, the measurement technique for vertical displacement, which utilizes target tracking through computer vision algorithms, is applicable for analysing the motion of models while lowering the expenses associated with conducting experiments in wave flumes. Furthermore, it has been demonstrated that this technique can effectively measure 2D waves, even in the presence of non-linearities, and can be compared against numerical model simulations.

Author Contributions: Conceptualization, S.C.M. and C.G.S.; Methodology, S.C.M., P.A. and I.B.d.S.B.; writing—original manuscript, S.C.M., P.A., I.B.d.S.B. and C.G.S. All authors have read and agreed to the published version of the manuscript.

Funding: This work was performed within the project Hydroelastic behaviour of horizontal flexible floating structures for applications to Floating Breakwaters and Wave Energy Converters (HYDROELASTWEB), which is co-funded by the European Regional Development Fund (Fundo Europeu de Desenvolvimento Regiona—FEDER) and by the Portuguese Foundation for Science and Technology (Fundação para a Ciência e a Tecnologia—FCT) under contract 031488_770 (PTDC/ECI-EGC/31488/2017). The first author has been contracted as a Researcher by the Portuguese Foundation for Science and Technology (Fundação para a Ciência e Tecnologia—FCT) through Scientific Employment Stimulus, Individual Support under contract No. CEECIND/04879/2017. The second author has been funded by the Portuguese Foundation for Science and Technology (Fundação para a Ciência e a Tecnologia—FCT) through a doctoral fellowship under the contract no. UI/BD/154592/2023. This work contributes to the Strategic Research Plan of the Centre for Marine Technology and Ocean Engineering (CENTEC), which is financed by the Portuguese Foundation for Science and Technology (Fundação para a Ciência e Tecnologia—FCT) under contract UIDB/UIDP/00134/2020.

Institutional Review Board Statement: Not applicable.

Informed Consent Statement: Not applicable.

Data Availability Statement: Data are contained within the article.

Conflicts of Interest: The authors declare no conflicts of interest.

Abbreviations

BEM	Boundary Element Method
BIEM	Boundary Integral Equation Method
BVP	Boundary Value Problem
CFD	Computational Fluid Dynamics
DOF	Degree of Freedom
DE-FE	Discrete Module–Finite Element
EVA	Ethylene Vinyl Acetate
FD	Frequency Domain
FEM	Finite Element Method
FFS	Floating Flexible Structure
FPS	Frames per Second
RAO	Response Amplitude Operator
SWL	Still Water Level
TD	Time Domain
VLFS	Very Large Floating Structure
WEC	Wave Energy Conversion
WG	Wave Gauge

References

1. Wang, Q.; He, C.; Ding, J.; Geng, Y.; Cheng, X.; Zhang, X.; Ni, X.; Wang, J.; Wu, Y. Numerical and experimental studies on the dynamic responses of a multiply-connected domain tourism platform in head waves. *Ocean Eng.* **2024**, *294*, 116795. [CrossRef]
2. Flikkema, M.; Breuls, M.; Jak, R.; de Ruijter, R.; Drummen, I.; Jordaens, A.; Adam, F.; Czapiewska, K.; Lin, F.Y.; Schott, D.; et al. *Floating Island Development and Deployment Roadmap*; Technical Report; Space@Sea: Wageningen, The Netherlands, 2021.
3. Waals, O.J.; Bunnik, T.H.J.; Otto, W.J. Model tests and numerical analysis for a floating Mega Island. In Proceedings of the ASME 2018 37th International Conference on Ocean, Offshore and Arctic Engineering, Madrid, Spain, 17–22 June 2018.
4. Bi, C.W.; Ma, C.; Zhao, Y.P.; Xin, L.X. Physical model experimental study on the motion responses of a multi-module aquaculture platform. *Ocean Eng.* **2021**, *239*, 109862. [CrossRef]
5. Riggs, H.; Ertekin, R. Approximate methods for dynamic response of multi-module floating structures. *Marine Struct.* **1993**, *6*, 117–141. [CrossRef]
6. Diamantoulaki, I.; Angelides, D.C. Analysis of the performance of hinged floating breakwaters. *Eng. Struct.* **2010**, *32*, 2407–2423. [CrossRef]
7. Jiang, C.; el Moctar, O.; Schellin, T.E. Hydrodynamic Sensitivity of Moored and Articulated Multibody Offshore Structures in Waves. *J. Mar. Sci. Eng.* **2021**, *9*, 1028. [CrossRef]
8. Wu, Y.S.; Ding, J.; Tian, C.; Li, Z.W.; Ling, H.J.; Ma, X.Z.; Gao, J.L. Numerical analysis and model tests of a three-module VLFS deployed near islands and reefs. *J. Ocean Eng. Mar. Eng.* **2018**, *4*, 111–122. [CrossRef]
9. Jin, C.; Bakti, F.P.; Kim, M.H. Multi-floater-mooring coupled time-domain hydro-elastic analysis in regular and irregular waves. *Appl. Ocean Res.* **2020**, *101*, 102276. [CrossRef]
10. Lu, D.; Fu, S.; Zhang, X.; Guo, F.; Gao, Y. A method to estimate the hydroelastic behaviour of VLFS based on multi-rigid-body dynamics and beam bending. *Ships Offshore Struct.* **2016**, *14*, 354–362. [CrossRef]
11. Xu, D.L.; Zhang, H.C.; Xia, S.Y.; Lu, C.; Qi, E.R.; Tian, C.; Wu, Y.S. Nonlinear dynamic characteristics of a multi-module floating airport with rigid-flexible connections. *J. Hydrody.* **2018**, *30*, 815–827. [CrossRef]
12. Zhao, C.; Hao, X.; Liang, R.; Lu, J. Influence of hinged conditions on the hydroelastic response of compound floating structures. *Ocean Eng.* **2015**, *101*, 12–24. [CrossRef]
13. Yoon, J.; Cho, S.; Jiwinangun, R.G.; Lee, P. Hydroelastic analysis of floating plates with multiple hinge connections in regular waves. *Marine Struct.* **2014**, *36*, 65–87. [CrossRef]
14. Zhang, X.; Lu, D.; Gao, Y.; Chen, L. A time domain discrete-module-beam-bending-based hydroelasticity method for the transient response of very large floating structures under unsteady external loads. *Ocean Eng.* **2018**, *164*, 332–349. [CrossRef]
15. Mohapatra, S.C.; Guedes Soares, C. Effect of mooring lines on the hydroelastic response of a floating flexible plate using the BIEM approach. *J. Mar. Sci. Eng.* **2021**, *9*, 941. [CrossRef]
16. Mohapatra, S.C.; Guedes Soares, C. Hydroelastic Response of a Moored Floating Flexible Circular Structure Applying BIEM. *J. Mar. Sci. Eng.* **2023**, *11*, 2322. [CrossRef]

17. Chu, Y.I.; Wang, C.M.; Zhang, H. A frequency domain approach for analyzing motion responses of integrated offshore fish cage and wind turbine under wind and wave actions. *Aqua. Eng.* **2022**, *97*, 102241. [CrossRef]
18. Cheng, Y.; Zhai, G.; Ou, J. Numerical and experimental analysis of hydroelastic response on a very large floating structure edged with a pair of submerged horizontal plates. *J. Mar. Sci. Tech.* **2015**, *20*, 127–141. [CrossRef]
19. Cheng, Y.; Ji, C.; Zhai, G.; Gaidai, O. Hydroelastic analysis of oblique irregular waves with a pontoon-type VLFS edged with dual inclined perforated plates. *Marine Struct.* **2016**, *49*, 31–57. [CrossRef]
20. Shi, Q.; Xu, D.; Zhang, H.; Zhao, H.; Ding, J.; Wu, Y. A face-contact connector for modularized floating structures. *Marine Struct.* **2022**, *82*, 103149. [CrossRef]
21. Jiang, S.C.; Bai, W.; Tang, G.Q. Numerical simulation of wave resonance in the narrow gap between two non-identical boxes. *Ocean Eng.* **2018**, *156*, 38–60. [CrossRef]
22. Gao, J.L.; He, Z.W.; Huang, X.H.; Liu, Q.; Zang, J.; Wang, G. Effects of free heave motion on wave resonance inside a narrow gap between two boxes under wave actions. *Ocean Eng.* **2021**, *224*, 108753. [CrossRef]
23. Gong, S.; Gao, J.; Song, Z.; Shi, H.; Liu, Y. Hydrodynamics of fluid resonance in a narrow gap between two boxes with different breadths. *Ocean Eng.* **2024**, *311 Pt 2*, 118986. [CrossRef]
24. Gao, S.; Cong, P.; Teng, B. Effect of incident wave angle to gap resonance between two fixed barges. *Ocean Eng.* **2022**, *257*, 111583. [CrossRef]
25. Gao, J.; Mi, C.; Song, Z.; Liu, Y. Transient gap resonance between two closely-spaced boxes triggered by nonlinear focused wave groups. *Ocean Eng.* **2024**, *305*, 117938. [CrossRef]
26. Ran, Y.Q.; Jiang, S.C.; Geng, B.L.; Jin, R.J. Hydrodynamic behavior of gap resonance in multiple-box systems with sharp and round inlet configurations. *China Ocean Eng.* **2023**, *37*, 849–862. [CrossRef]
27. Chen, Y.; Zhang, X.; Shen, K.; Ren, X. Extension of the discrete-module-finite-element method into the interconnected large floating flexible structures. *Ocean Eng.* **2023**, *269*, 113549. [CrossRef]
28. Song, Z.; Jiao, Z.; Gao, J.; Mi, C.; Liu, Y. Numerical investigation on the hydrodynamic wave forces on the three barges in proximity. *Ocean Eng.* **2025**, *316*, 119941. [CrossRef]
29. Mi, C.; Gao, J.; Song, Z.; Liu, Y. Hydrodynamic wave forces on two side-by-side barges subjected to nonlinear focused wave groups. *Ocean Eng.* **2025**, *317*, 120056. [CrossRef]
30. Kagemoto, H.; Fujino, M.; Murai, M. Theoretical and experimental predictions of the hydroelastic response of a very large floating structure in waves. *Appl. Ocean Res.* **1998**, *20*, 135–144. [CrossRef]
31. Cui, J.; Liu, H.; Deng, X.; Tao, S.; Li, Q. An experimental study on hydrodynamic performance of a box-floating breakwater in different terrains. *J. Mar. Sci. Tech.* **2020**, *25*, 991–1009. [CrossRef]
32. Ding, J.; Geng, Y.C.; Xu, S.W.; Yang, W.N.; Xie, Z.Y. Experimental study on responses of an 8-module VLFS considering different encounter wave conditions. *Marine Struct.* **2021**, *78*, 102959. [CrossRef]
33. Ding, R.; Zhang, H.; Liu, C.; Xu, D.; Shi, Q.; Liu, J.; Zou, W.; Wu, U. Connector configuration effect on the dynamic characteristics of multi-modular floating structure. *J. Ocean Eng. Sci.* **2022**, *9*, 517–527. [CrossRef]
34. Bispo, I.B.S.; Amouzadrad, P.; Mohapatra, S.C.; Guedes Soares, C. Motion analysis of a floating horizontal set of interconnected plates based on computer vision target tracking technique. In *Advances in the Analysis and Design of Marine Structures*; Ringsberg, J.W., Guedes Soares, C., Eds.; Taylor and Francis: London, UK, 2023; pp. 153–159.
35. Perić, M.; Swan, C. An experimental study of the wave excitation in the gap between two closely spaced bodies, with implications for LNG offloading. *Appl. Ocean Res.* **2015**, *51*, 320–330. [CrossRef]
36. Zhao, W.; Wolgamot, H.A.; Taylor, P.H. Gap resonance and higher harmonics driven by focused transient wave groups. *J. Fluid Mech.* **2017**, *812*, 905–939. [CrossRef]
37. Zhang, D.Q.; Yuan, Z.M.; Zhao, G.W.; Chen, Y.J.; Du, J.F. An Experimental and Numerical Study of Motion Responses of Multi-Body Arrays with Hinge Connections. *J. Mar. Sci. Eng.* **2024**, *12*, 1791. [CrossRef]
38. Ding, J.; Wu, Y.; Zhou, Y.; Ma, X.; Ling, H.; Xie, Z. Investigation of connector loads of a 3-module VLFS using experimental and numerical methods. *Ocean Eng.* **2020**, *195*, 106684. [CrossRef]
39. Ding, J.; Xie, Z.; Wu, Y.; Xu, S.; Qiu, G.; Wang, Y.; Wang, Q. Numerical and experimental investigation on hydroelastic responses of an 8-module VLFS near a typical island. *Ocean Eng.* **2020**, *214*, 107841. [CrossRef]
40. Sun, B.; Li, C.; Yang, S.; Zhang, H.; Song, Z. Experimental and numerical study on the wave energy dissipation and dynamic response of kelp-box type floating breakwater. *Ocean Eng.* **2022**, *263*, 112374. [CrossRef]
41. Chen, M.; Ouyang, M.; Guo, H.; Zou, M.; Zhang, C.A. Coupled Hydrodynamic–Structural Model for Flexible Interconnected Multiple Floating Bodies. *J. Mar. Sci. Eng.* **2023**, *11*, 813. [CrossRef]
42. Song, X.; Liu, W.; Wu, H. Investigation on Load Characteristics of Hinged Connector for a Large Floating Structure Model under Wave Actions. *J. Mar. Sci. Eng.* **2023**, *11*, 786. [CrossRef]
43. Amouzadrad, P.; Mohapatra, S.C.; Guedes Soares, C. Review of recent developments on the hydroelastic response and gap resonance of multi-body floating structures. *Ocean Eng.* **2024**, *313*, 119398. [CrossRef]

44. Bispo, I.B.S.; Mohapatra, S.C.; Guedes Soares, C. Numerical analysis of a moored very large floating structure composed by a set of hinged plates. *Ocean Eng.* **2022**, *253*, 110785. [CrossRef]
45. ANSYS, Inc. *AQWA Theory Manual*; ANSYS, Inc.: Canonsburg, PA, USA, 2020.
46. Chakrabarti, S.K. Offshore Structure Modeling. In *Advanced Series on Ocean Engineering*; World Scientific: Singapore, 1994; Volume 9, ISBN 9810215134.
47. Mohapatra, S.C.; Guo, Y.C.; Guedes Soares, C. Analytical and experimental study on wave interaction with a horizontal floating flexible membrane supported by linear springs. In *Trends in Renewable Energies Offshore*; Guedes Soares, C., Ed.; CRC Press: Boca Raton, FL, USA; Taylor & Francis Group: London, UK, 2023; pp. 257–266.
48. Dean, R.G.; Dalrymple, R.A. *Water Wave Mechanics for Engineers and Scientists*; Advanced Series in Ocean Engineering; World Scientific Publishing, Co., Ltd.: Singapore, 1984; Volume 2.
49. Mohapatra, S.C.; Guedes Soares, C.; Belibassakis, K. Current Loads on a Horizontal Floating Flexible Membrane in a 3D Channel. *J. Mar. Sci. Eng.* **2024**, *12*, 1583. [CrossRef]
50. Amouzadrad, P.; Mohapatra, S.C.; Guedes Soares, C. Effect of current on the hydroelastic behavior of floating flexible circular structure. *Appl. Ocean Res.* **2025**, *154*, 104387. [CrossRef]

Disclaimer/Publisher's Note: The statements, opinions and data contained in all publications are solely those of the individual author(s) and contributor(s) and not of MDPI and/or the editor(s). MDPI and/or the editor(s) disclaim responsibility for any injury to people or property resulting from any ideas, methods, instructions or products referred to in the content.